

Optimized superconductivity in the vicinity of a nematic quantum critical point in the kagome superconductor $\text{Cs}(\text{V}_{1-x}\text{Ti}_x)_3\text{Sb}_5$

Received: 15 March 2023

Accepted: 6 June 2023

Published online: 06 July 2023

 Check for updatesYeahan Sur¹, Kwang-Tak Kim¹, Sukho Kim¹ & Kee Hoon Kim^{1,2}✉

CsV_3Sb_5 exhibits superconductivity at $T_c = 3.2$ K after undergoing intriguing two high-temperature transitions: charge density wave order at ~ 98 K and electronic nematic order at $T_{\text{nem}} \sim 35$ K. Here, we investigate nematic susceptibility in single crystals of $\text{Cs}(\text{V}_{1-x}\text{Ti}_x)_3\text{Sb}_5$ ($x = 0.00\text{--}0.06$) where double-dome-shaped superconducting phase diagram is realized. The nematic susceptibility typically exhibits the Curie–Weiss behaviour above T_{nem} , which is monotonically decreased with x . Moreover, the Curie–Weiss temperature is systematically suppressed from ~ 30 K for $x = 0$ to ~ 4 K for $x = 0.0075$, resulting in a sign change at $x = -0.009$. Furthermore, the Curie constant reaches a maximum at $x = 0.01$, suggesting drastically enhanced nematic susceptibility near a putative nematic quantum critical point (NQCP) at $x = -0.009$. Strikingly, T_c is enhanced up to ~ 4.1 K with full Meissner shielding realized at $x = -0.0075\text{--}0.01$, forming the first superconducting dome near the NQCP. Our findings directly point to a vital role of nematic fluctuations in enhancing the superconducting properties of $\text{Cs}(\text{V}_{1-x}\text{Ti}_x)_3\text{Sb}_5$.

Metals with kagome lattices have drawn enormous attention due to their unique electronic structures, which can host Dirac points, flat bands, and saddle points in their crystal momentum space. Many of these peculiar features can lead to electronic instabilities associated with divergence in the density of states near the Fermi level. As such, it has been theoretically predicted that various emergent orders such as charge bond order^{1,2}, charge density wave (CDW) order¹, nematic order³, and superconductivity^{1,2,4} might appear. For instance, a functional renormalisation group study on the kagome-Hubbard model predicted that CDW order and unconventional d -wave superconductivity can arise near a van Hove singularity at an electron filling of $5/4$ per band¹.

Recently discovered V-based kagome metals AV_3Sb_5 ($A = \text{K}, \text{Rb}, \text{and Cs}$) represent experimental realisations of these various theoretical predictions; each member indeed exhibits signatures of the structural transition due to the CDW order below its CDW transition temperature T_{CDW} , where $T_{\text{CDW}} = 80\text{--}104$ K^{5–7}, followed by the coexistence of superconductivity^{8–10}. Within this material class, CsV_3Sb_5 has been most extensively studied due to its highest superconducting

transition temperature ($T_c = \sim 3.2$ K) and the presence of multiple structural and electronic instabilities. For example, the CDW order found at $T_{\text{CDW}} = 98$ K⁷ induces the first-order structural transition with a 2×2 modulation, showing a translational symmetry breaking in each kagome layer. Moreover, it was later found that the 2×2 modulation is accompanied by two kinds of out-of-plane modulations (i.e., $2 \times 2 \times 2^{11}$ and $2 \times 2 \times 4^{12}$). The structure in the CDW states with the c -axis modulation is compatible with the C_2 rotational symmetry below T_{CDW} ¹³. However, it is known that the electronic rotational symmetry in each kagome layer is still maintained as C_6 just below T_{CDW} ¹⁴. With a further decrease in temperature, the system finally reaches the electronic nematic transition at $T_{\text{nem}} \sim 35$ K, at which a rotational symmetry of the electronic state is continuously varied from C_6 to C_2 in the kagome layer, as evidenced by nuclear magnetic resonance (NMR), scanning tunnelling microscopy and elastoresistance measurements¹⁴.

Alongside the experimental progresses, recent theoretical studies based on the kagome-Hubbard model have successfully explained the multiple thermal phase transitions related to the CDW and the nematic orders in CsV_3Sb_5 ^{3,15–18}. Namely, the charge ordering at T_{CDW} is

¹Center for Novel States of Complex Materials Research, Department of Physics and Astronomy, Seoul National University, Seoul 08826, Republic of Korea.

²Institute of Applied Physics, Department of Physics and Astronomy, Seoul National University, Seoul 08826, Republic of Korea. ✉e-mail: optopia@snu.ac.kr

understood as stemming from a triple- \mathbf{q} -charge bond order, arising from the Fermi surface nesting at the van Hove singularity points in CsV_3Sb_5 ^{3,15}. Moreover, near the suppression of these charge bond orders, it has been predicted that bond order fluctuations can mediate sizable pairing glue for superconductivity, possibly resulting in the superconductivity of various symmetries including singlet s -wave¹⁷, triplet p -wave¹⁷, or d -wave superconductivity¹.

However, in spite of extensive progress in both experiments and theories, the superconducting properties of CsV_3Sb_5 are still poorly understood. Firstly, no consensus has been reached on the pairing symmetry of CsV_3Sb_5 . While unconventional superconductivity with the nodal gap structure has been suggested by thermal conductivity¹⁹ and scanning tunnelling microscopy data²⁰, tunnel diode oscillator²¹ and muon spin resonance measurements²² support a nodeless s -wave gap with a sign-preserving order parameter. Secondly, an unusual superconducting phase diagram with a double-dome shape has been found independently either as a function of Sn doping in $\text{CsV}_3\text{Sb}_{5-x}\text{Sn}_x$ polycrystals²³ or that of pressure in a CsV_3Sb_5 single crystal^{24,25}, of which physical mechanisms remain elusive.

Elastoresistance measurements, which is a direct probe of the even-parity nematic susceptibility, have been found to be quite useful in unravelling the pivotal role of nematic fluctuation in mediating Cooper pairing, particularly in several Fe-based superconductors^{26–30}. To better understand the role of nematic order in the superconductivity of CsV_3Sb_5 , we employ elastoresistance measurements to systematically study the nematic susceptibility in high-quality single

crystals of Ti-doped CsV_3Sb_5 , $\text{Cs}(\text{V}_{1-x}\text{Ti}_x)_3\text{Sb}_5$. It should be emphasised that such studies have not been available thus far, as both controlling the doping ratios and maintaining high quality in the doped single crystals of CsV_3Sb_5 have been quite challenging^{31,32}.

Results

Figure 1a depicts the crystal structure of CsV_3Sb_5 , forming the hexagonal $P6/mmm$ space group with lattice constants of $a = b = 5.508 \text{ \AA}$ and $c = 9.326 \text{ \AA}$. One unit cell comprises a V-Sb layer sandwiched by Cs atoms. Within each V-Sb sheet, a kagome network of V atoms is interlaced with a hexagonal lattice of Sb. As the temperature is lowered below $T_{\text{CDW}} = 98 \text{ K}$, the V atoms rearrange themselves to form an inverse star-of-David pattern (2×2 charge order) in the kagome plane^{7,33}. As the temperature is lowered further, an additional ordering is known to appear at $T_{\text{nem}} \sim 35 \text{ K}$, below which the system forms a distinct nematic phase¹⁴ (Fig. 1b). Upon Ti doping, the titanium atoms can occupy the vanadium sites, resulting in progressive distortion of the vanadium kagome network.

Figure 1c shows the in-plane resistivity ρ_{ab} of $\text{Cs}(\text{V}_{1-x}\text{Ti}_x)_3\text{Sb}_5$ normalised by the resistivity at 300 K ($\rho_{ab}/\rho_{ab,300 \text{ K}}$). The resistivity of the undoped CsV_3Sb_5 , evidencing metallic behaviour near room temperature, exhibits a slight shoulder near 98 K due to the formation of the CDW order. With increasing x , the residual resistivity ratio (RRR) of $\text{Cs}(\text{V}_{1-x}\text{Ti}_x)_3\text{Sb}_5$ systematically decreases. This result implies increased impurity scattering within the kagome plane in proportion to x . Along

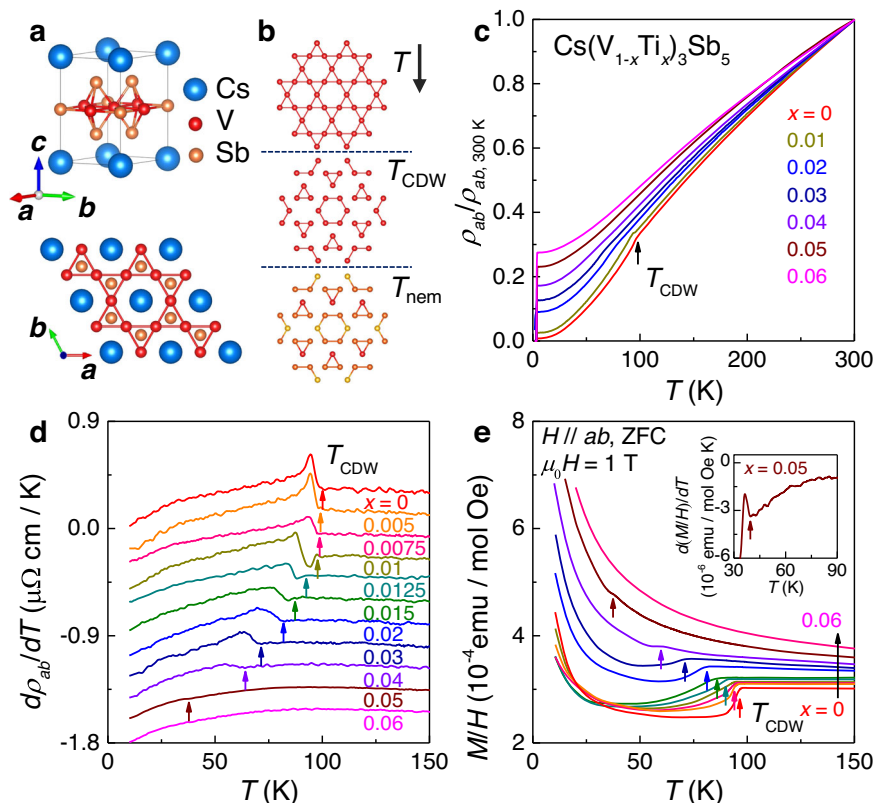


Fig. 1 | Structure, in-plane resistivity (ρ_{ab}) and magnetic susceptibility (M/H) of $\text{Cs}(\text{V}_{1-x}\text{Ti}_x)_3\text{Sb}_5$. a The crystal structure of CsV_3Sb_5 . In the V_3Sb_5 layer, vanadium atoms form a kagome network within the ab plane. **b** Schematic illustration of the temperature-dependent evolution of the vanadium kagome net across the known phase transitions of CsV_3Sb_5 . Here, the T_{CDW} indicates the charge density wave (CDW) transition temperature, while T_{nem} indicates the nematic transition temperature. The red (orange) coloured vanadium atoms describe the maximum (minimum) of the local electron density of states in the nematic state, as observed from differential conductance maps from a recent scanning tunnelling microscopy

experiment¹⁴. **c** Temperature dependence of the in-plane resistivity (ρ_{ab}) normalised by the resistivity value of $\text{Cs}(\text{V}_{1-x}\text{Ti}_x)_3\text{Sb}_5$ single crystals at 300 K for $0 \leq x \leq 0.06$. **d** $d\rho_{ab}/dT$ curves of $\text{Cs}(\text{V}_{1-x}\text{Ti}_x)_3\text{Sb}_5$. The curves have been vertically shifted for clarity. The coloured arrows indicate T_{CDW} . **e** Temperature dependence of the M/H of $\text{Cs}(\text{V}_{1-x}\text{Ti}_x)_3\text{Sb}_5$ measured at a constant external field of $\mu_0 H = 1 \text{ T}$ after zero-field cooling (ZFC). Here, M and H indicate the magnetisation and magnetic field, respectively. The inset depicts the temperature-dependent $d(M/H)/dT$ plot of $\text{Cs}(\text{V}_{0.95}\text{Ti}_{0.05})_3\text{Sb}_5$ near T_{CDW} .

with the decreased RRR value, $\text{Cs}(\text{V}_{1-x}\text{Ti}_x)_3\text{Sb}_5$ exhibits increasingly broadened CDW transitions with increasing x , which are well visualised in the $d\rho_{ab}/dT$ curves (Fig. 1d). Furthermore, the anomalies in $d\rho_{ab}/dT$ shift to lower temperatures, indicating the development of a lower T_{CDW} at higher x , e.g., -59 K at $x = 0.04$. The decreasing trend of T_{CDW} is also confirmed by the dc magnetic susceptibility (M/H) data presented in Fig. 1e. A drop in the M/H curve observed in pristine CsV_3Sb_5 , a Pauli paramagnet, indicates that depletion of the density of states has occurred due to the CDW gap opening at $T_{\text{CDW}} = 98$ K. Consistent with the behaviour found in ρ_{ab} , increasing x results in a shift in T_{CDW} (the temperature of the M/H drop) to lower temperatures as well as a progressively decreased and broadened drop. This indicates that with progressive perturbation in the V atom arrangement by Ti doping, depletion of the electronic density of states at the long-range CDW transition is systematically reduced along with the decrease of the averaged T_{CDW} and the increase of the T_{CDW} distribution.

As the systematic suppression of T_{CDW} is established with Ti doping, we now turn to the evolution of superconductivity to understand its interplay with the pre-existing CDW order. Figure 2 shows low-temperature $\rho_{ab}(T)$ and $4\pi\chi(T)$ data of $\text{Cs}(\text{V}_{1-x}\text{Ti}_x)_3\text{Sb}_5$. T_c is clearly identified by either zero resistivity or the onset of diamagnetic behaviour in the $\chi(T)$ curves. Here, we define T_c from the transport data by the criterion of $0.5\rho_N$ (ρ_N : normal-state resistivity)³⁴. It is noted that T_c exhibits nonmonotonic behaviour with x . At $x = 0.0075$, T_c is maximised to 4.1 K from $T_c = 3.2$ K for the pristine compound. Moreover, in the doping range of $x = 0.0-0.01$, a full Meissner shielding of $-4\pi\chi \cong 1$ is realised. However, with a further increase of x towards $x = 0.02$, T_c is progressively suppressed to -1.9 K, accompanied by decreased Meissner shielding of $-4\pi\chi \cong 0.3$ at $x = 0.015$ and $-4\pi\chi \cong 0$ around $x = 0.02$. At $x > 0.02$, T_c increases again to 3.8 K at $x = 0.05$ and recovers the full Meissner shielding. Thus, the evolution of the superconducting properties, i.e., T_c and Meissner shielding, reveals a double-dome feature.

Finding a superconducting region with a double-dome feature among CDW materials is unusual because the competition between CDW and superconductivity often leads to either a monotonically extended region of superconductivity after the collapse of the CDW order³⁵, or a single superconducting dome stabilised at the putative CDW quantum critical point (QCP)³⁶. While an increase in T_c at $x = -0.05$ may be associated with the putative QCP of the CDW order,

identifying another superconducting dome within the CDW order is truly uncommon. This finding strongly suggests that additional fluctuating orders could be present, enhancing the pairing interaction.

To investigate the origin of the unusual trend in T_c , the elastoresistance in $\text{Cs}(\text{V}_{1-x}\text{Ti}_x)_3\text{Sb}_5$ was investigated from 6 to 250 K. Figure 3a illustrates the experimental configuration for the elastoresistance measurements. It is known that nematic susceptibility \tilde{n} can be obtained by measuring the electronic anisotropy induced by anisotropic strain. In other words, \tilde{n} becomes linearly proportional to the anisotropic change in the resistance $N \equiv (\Delta R/R)_{xx} - (\Delta R/R)_{yy}$ in response to anisotropic strain $(\epsilon_{xx} - \epsilon_{yy})$, which results in $\tilde{n} = \alpha \partial N / \partial (\epsilon_{xx} - \epsilon_{yy})$. Here, α is a proportionality constant depending on microscopic details of the electronic structure³⁷ (See, Supplementary Note 8, for details). Therefore, $\partial N / \partial (\epsilon_{xx} - \epsilon_{yy})$ reveals the essential temperature dependence of \tilde{n} upon approaching a thermally driven nematic phase transition. According to the general definition of elastoresistance coefficients $(\Delta R/R)_i \equiv \sum_{j=1}^6 m_{ij} \epsilon_j$ ³⁷, $\partial N / \partial (\epsilon_{xx} - \epsilon_{yy})$ can be expressed in terms of m_{ij} , where ϵ_j represents the engineering strain, m_{ij} are elastoresistance tensor components, and the subscripts i and j represent the Voigt notation ($1 = xx, 2 = yy, 3 = zz, 4 = yz, 5 = zx, 6 = xy$). For a crystal in the D_{6h} point group with x measured along the $[100]$ axis¹⁴, $\partial N / \partial (\epsilon_{xx} - \epsilon_{yy})$ directly corresponds to the elastoresistance coefficient $(m_{11} - m_{12})$, representing the nematic susceptibility \tilde{n} along the even-parity E_{2g} symmetry channel (See, Supplementary Note 4).

Figure 3b depicts the response of N to $(\epsilon_{xx} - \epsilon_{yy})$ for CsV_3Sb_5 at selected temperatures. N shows a linear relationship with $(\epsilon_{xx} - \epsilon_{yy})$, enabling a precise measurement of \tilde{n} by obtaining $N / (\epsilon_{xx} - \epsilon_{yy})$ in a small strain limit of $(\epsilon_{xx} - \epsilon_{yy}) \rightarrow 0$. This parameter is redefined as $\tilde{n} = \partial N / \partial (\epsilon_{xx} - \epsilon_{yy})$ (α is set to be 1), and the resulting $\tilde{n}(T)$ curve for CsV_3Sb_5 is presented in the top panel of Fig. 3c. A sharp jump in \tilde{n} is found at $T_{\text{CDW}} = 98$ K, implying that the first-order structural transition³⁸ due to the charge bond order results in an abrupt offset change in the elastoresistance anisotropy. It is found that at temperatures above 36 K and below the sharp jump near T_{CDW} , \tilde{n} is well fitted by the Curie–Weiss-type temperature dependence,

$$\tilde{n} = \tilde{n}_0 + \frac{C}{T - \theta_{\text{nem}}}. \quad (1)$$

Here, \tilde{n}_0 describes the intrinsic anisotropy in the piezoresistivity effect, unrelated to electronic nematicity, θ_{nem} is the mean-field nematic transition temperature, and C is the Curie constant of the corresponding nematic susceptibility. A good agreement of the experimental data to Eq. (1) can be confirmed by a fitted red solid line with $\theta_{\text{nem}} = 30$ K, $\tilde{n}_0 = 14.7$, and $C = 39$ K. A good fit to Eq. (1) can also be verified by the plots of $(\tilde{n} - \tilde{n}_0)^{-1}$ and $(\tilde{n} - \tilde{n}_0)(T - \theta_{\text{nem}})$ at the bottom panel of Fig. 3c, which exhibit linear (pink open circles) and constant (green open circles) behaviours with temperature, respectively. The nearly constant value of $(\tilde{n} - \tilde{n}_0)(T - \theta_{\text{nem}})$ should directly correspond to the C value.

It should be further noted in Fig. 3c that below 36 K as represented by a black dotted line, the experimental data clearly deviate from the trace predicted by Eq. (1). This deviation indicates that the nematic correlation goes beyond the mean-field description below this temperature located near the long-range ordering temperature T_{nem} . The temperature of 36 K is indeed close to $T_{\text{nem}} \sim 35$ K, as found by the previous work¹⁴. Therefore, our observation shows that a significant nematic correlation of even-parity type exists above T_{nem} up to T_{CDW} and even above T_{CDW} (vide infra).

Similar measurements and analyses were performed for $\text{Cs}(\text{V}_{1-x}\text{Ti}_x)_3\text{Sb}_5$ up to $x = 0.06$ (Fig. 3d–i) (for plots with $x \geq 0.03$, see Supplementary Fig. 6). It is noted that the jump in \tilde{n} at T_{CDW} systematically decreases with increasing x , indicating weakened elastoresistance anisotropy at the CDW ordering. More importantly, we find that

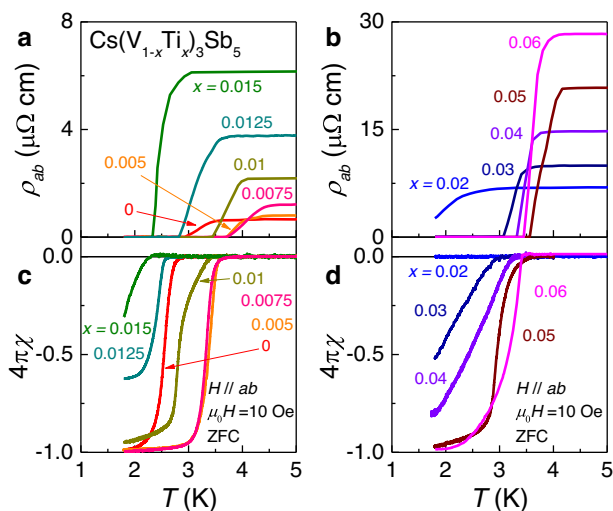


Fig. 2 | Superconducting properties of $\text{Cs}(\text{V}_{1-x}\text{Ti}_x)_3\text{Sb}_5$. Low-temperature behaviour of the in-plane resistivity ρ_{ab} in $\text{Cs}(\text{V}_{1-x}\text{Ti}_x)_3\text{Sb}_5$ for **a** $0 \leq x \leq 0.015$ and **b** $0.02 \leq x \leq 0.06$. Temperature dependence of $4\pi\chi$ (χ : magnetic susceptibility) measured at $\mu_0 H = 10$ Oe after zero-field cooling (ZFC) for **c** $0 \leq x \leq 0.015$ and **d** $0.02 \leq x \leq 0.06$.

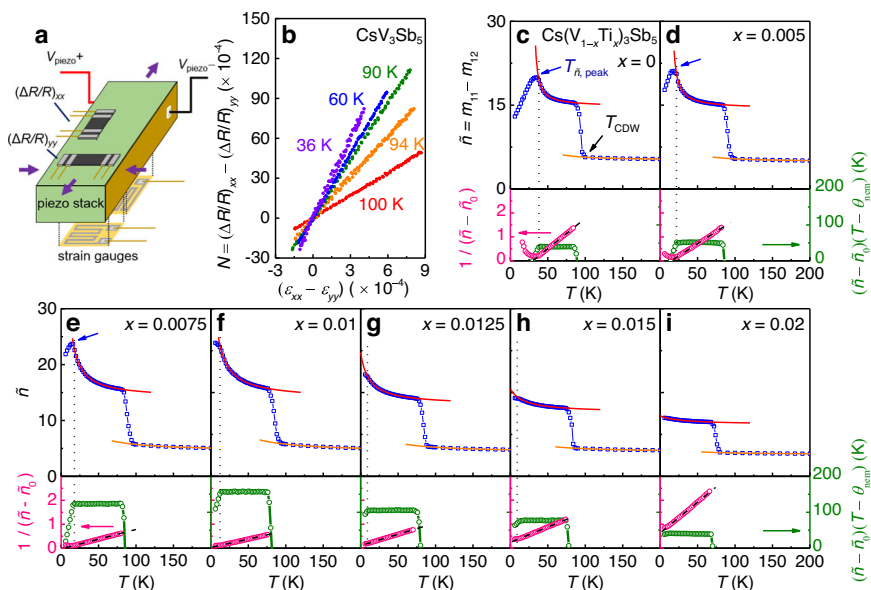


Fig. 3 | Experimental methods for nematic susceptibility measurements and the temperature-dependent nematic susceptibility in $\text{Cs}(\text{V}_{1-x}\text{Ti}_x)_3\text{Sb}_5$.

a Schematic illustration of the elastoresistance measurement setup. Here, V_{piezo} indicates the voltage applied on the piezo stack. **b** N vs. $(\epsilon_{xx} - \epsilon_{yy})$ plot of CsV_3Sb_5 at several representative temperatures, exhibiting a linear relationship; the nematic susceptibility \tilde{n} can be obtained as $\partial N / \partial (\epsilon_{xx} - \epsilon_{yy})$. **c–i** (top panel) Temperature dependence of \tilde{n} in $\text{Cs}(\text{V}_{1-x}\text{Ti}_x)_3\text{Sb}_5$ for $0 \leq x \leq 0.02$. A sharp jump in \tilde{n} is observed

near T_{CDW} . Below and above this jump, the data can be clearly fitted to the Curie–Weiss formula (Eq. (1)) (red and orange solid lines, respectively). The black dotted line indicates the deviation temperature from a Curie–Weiss fit, while the blue arrow indicates the peak temperature of \tilde{n} , $T_{\tilde{n}, \text{peak}}$. **c–i** (bottom panel) Temperature dependence of $(\tilde{n} - \tilde{n}_0)^{-1}$ and $(\tilde{n} - \tilde{n}_0)(T - \theta_{\text{nem}})$ below T_{CDW} , represented by the pink and green open circles, respectively. The black dashed line refers to a linear guideline.

all the samples up to $x=0.03$ exhibit the Curie–Weiss temperature dependence of \tilde{n} in broad temperature ranges above deviation temperatures represented by black dotted lines. For $x=0–0.0075$, \tilde{n} data clearly develop a peak at $T_{\tilde{n}, \text{peak}}$. In previous work on the pristine sample¹⁴, T_{nem} identified by NMR and $T_{\tilde{n}, \text{peak}}$ determined by the \tilde{n} measurements were indeed nearly the same as ~ 35 K. Therefore, $T_{\tilde{n}, \text{peak}}$ can be used as a good estimate of T_{nem} for each doping³⁹. In our case, the resultant $T_{\tilde{n}, \text{peak}} = 34$ K for $x=0$ is indeed close to the known value of $T_{\text{nem}} = -35$ K¹⁴. For other x , $T_{\tilde{n}, \text{peak}}$ shows a monotonous decrease; $T_{\tilde{n}, \text{peak}} = 18$ K ($x=0.005$) and 14 K ($x=0.0075$). For $x=0.01$, however, we did not identify any peak feature at least down to 6 K, except finding the deviation temperature from the Curie–Weiss behaviour at ~ 12 K. This observation indicates that for $x=0.01$, the true long-range nematic ordering is located well below 6 K or might not even exist at a finite temperature. For $x=0.0125$ and 0.015 , $\tilde{n}(T)$ doesn't show any peak feature either, and only the deviation from the Curie–Weiss behaviour is identified around ~ 8 K. This indicates that in $x=0.0125$ and 0.015 , only nematic correlation exists without the development of true long-range order at a finite temperature.

In order to understand quantitatively the evolution of \tilde{n} over the broad doping ranges, we have tried to fit the experimental $\tilde{n}(T)$ of all the samples by Eq. (1) below T_{CDW} . (see Supplementary Table 2 for detailed fit parameters). Firstly, we discuss the evolution of C for each doping. In contrast to the monotonic decrease in the jump of $\tilde{n}(T)$ and $T_{\tilde{n}, \text{peak}}$ with x , C is found to exhibit nonmonotonic behaviour, i.e. increasing trend with x for $x=0–0.01$ and decreasing trend for $x \geq 0.0125$; C , as indicated by the slope of $(\tilde{n} - \tilde{n}_0)^{-1}$ or the value of $(\tilde{n} - \tilde{n}_0)(T - \theta_{\text{nem}})$, increases with x from $C = 39$ K ($x=0$) to 124 K ($x=0.0075$), and exhibits a maximum value of $C = \sim 157$ K at critical doping of $x_c = 0.01$. As a result, the highest value of $\tilde{n}(T = 6$ K) ~ 23.8 can be found at x_c . For $x \geq 0.0125$, C decreases with x to exhibit $C = 2$ K at $x=0.03$, resulting in a flattening of the $\tilde{n}(T)$ curve at higher doping ratios. For $x \geq 0.04$, Eq. (1) cannot be fitted very well to the $\tilde{n}(T)$ curves due to the almost temperature-independent behaviour below and above the T_{CDW} .

The fit to Eq. (1) strikingly reveals that θ_{nem} is systematically suppressed from 30.0 K ($x=0$) to 3.6 K ($x=0.0075$), and to eventually exhibit a sign change ($x = -0.009$). At higher x , θ_{nem} is suppressed further, resulting in $\theta_{\text{nem}} = -42$ K at $x=0.03$. In general, a nematic quantum critical point (NQCP) is often located at the phase space where θ_{nem} goes to zero temperature and strongly enhanced nematic susceptibility exists. The systematic suppression of θ_{nem} to zero temperature at $x = -0.009$, combined with the sharp maximum of the C value and the disappearance of $T_{\tilde{n}, \text{peak}}$ near x_c , strongly suggests the presence of an NQCP near the doping level close to $x \sim 0.009–0.01$. Indeed, similar phenomena have been observed in numerous Fe-based systems having the NQCP, such as $\text{Ba}(\text{Fe}_{1-x}\text{Co}_x)_2\text{As}_2$ ²⁷, $\text{Fe}(\text{Se}_{1-x}\text{S}_x)$ ²⁸, $\text{LaFe}_{1-x}\text{Co}_x\text{AsO}$ ²⁹, and $\text{Fe}(\text{Se}_{1-x}\text{Te}_x)$ ³⁰.

Another salient feature found in Fig. 3 is that the fit based on Eq. (1) below T_{CDW} for each doping level can be successfully extended to explain $\tilde{n}(T)$ above T_{CDW} with the same θ_{nem} and C but with a different \tilde{n}_0 (orange solid line). This observation indicates that the even-parity nematic correlation might persist even above T_{CDW} for CsV_3Sb_5 and $\text{Cs}(\text{V}_{1-x}\text{Ti}_x)_3\text{Sb}_5$ ($x \leq 0.03$). As a result, the Curie–Weiss tail above T_{CDW} becomes clearly visible for $0 \leq x \leq 0.03$, reaching at least up to the maximum investigated temperature of 250 K (see, Supplementary Fig. 6 for $\tilde{n}(T)$ plots up to 250 K and for $x \geq 0.03$). Because of the most enhanced C value, the Curie–Weiss tail of \tilde{n} becomes most conspicuous at $x_c = 0.01$. It is striking that the enhanced \tilde{n} up to at least 250 K is observed at $x_c = 0.01$ where the actual nematic ordering temperature is close to zero. This directly suggests that large quantum fluctuation of even-parity nematic order near the NQCP could be responsible for the enhancement of \tilde{n} at high temperatures.

Figure 4a, b summarises the phase diagram of $\text{Cs}(\text{V}_{1-x}\text{Ti}_x)_3\text{Sb}_5$ plotted on top of the colour contour of \tilde{n} ; T_{CDW} as derived from the data of ρ_{ab} (orange circles), M/H (yellow octagons), and \tilde{n} (brown crosses) are plotted for each x . Moreover, $T_{\tilde{n}, \text{peak}}$ (blue squares) and θ_{nem} (purple stars) obtained from \tilde{n} in Fig. 3 are plotted with the T_{nem} (pink cross) of $x=0$ determined in a previous work¹⁴. At $x=0$, a jump in $\tilde{n}(T)$ near T_{CDW} can be clearly identified by the abrupt change of colour

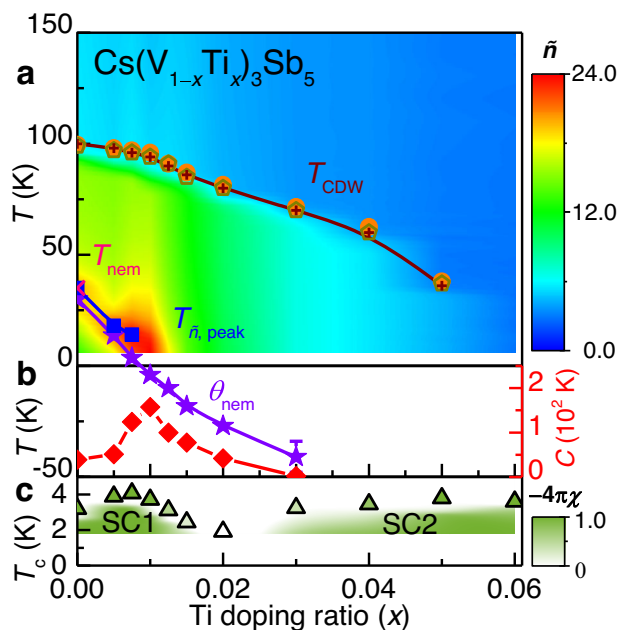


Fig. 4 | Colour contour plot of nematic susceptibility, analyses results of the Curie–Weiss fit, and electronic transition temperatures of $\text{Cs}(\text{V}_{1-x}\text{Ti}_x)_3\text{Sb}_5$. **a** The orange circles, yellow octagons, and brown crosses represent T_{CDW} obtained from ρ_{ab} , M/H , and \tilde{n} measurements. The pink cross in T_{nem} indicates the nematic transition temperature obtained from ref. 14. The blue squares and purple stars represent $T_{\tilde{n}, \text{peak}}$ and θ_{nem} obtained from the analysis of the nematic susceptibility \tilde{n} , respectively. A purple error bar is obtained by a standard deviation of the Curie–Weiss fit. The overlaid colour contour represents the interpolated values generated from \tilde{n} taken from the elastoresistance measurements. **b** The red diamonds show the Curie constant C obtained from the Curie–Weiss fits of \tilde{n} for $0 \leq x \leq 0.03$. **c** Superconducting transition temperature T_c (green triangles) defined by the criterion of $0.5\rho_N$ (ρ_N : normal-state resistivity) determined from Fig. 2. The colour contour represents the Meissner volume fraction ($-4\pi\chi$).

in \tilde{n} from blue at $T > T_{\text{CDW}}$ to green at $T < T_{\text{CDW}}$. Near T_{nem} , the contour exhibits a yellow colour, indicating a local maximum of \tilde{n} at $T_{\tilde{n}, \text{peak}}$. With an increase in doping, the $T_{\tilde{n}, \text{peak}}$ shifts to low temperatures, resulting in the most intensified \tilde{n} (6 K) indicated by the red colour near $x = 0.0075$ – 0.01 . This behaviour is also confirmed by the maximum of the C value, indicated by the red diamonds.

The superconducting phase diagram of $\text{Cs}(\text{V}_{1-x}\text{Ti}_x)_3\text{Sb}_5$ is also plotted in Fig. 4c. Here, the green triangles indicate the T_c obtained from transport measurements, while the Meissner volume fraction ($-4\pi\chi$) is represented below the trace of T_c as a green colour contour. Surprisingly, it is found that T_c is optimised to 4.1 K (3.7 K) near this doping range of $x = 0.0075$ – 0.01 , when the nematic correlations indicated by the \tilde{n} and C values are sharply enhanced near the NQCP. Our observation thus raises an intriguing possibility that fluctuation of the nematic order plays an important role in the pairing interaction to optimise superconductivity in the first superconducting dome of $\text{Cs}(\text{V}_{1-x}\text{Ti}_x)_3\text{Sb}_5$. At higher doping ratios of $0.01 \leq x \leq 0.02$, T_c is monotonically suppressed with doping, which could be related to the reduced nematic fluctuations as indicated by the decreased \tilde{n} and C values.

Based on our experimental findings and implications, the nematic fluctuations may be important in understanding the superconductivity in the AV_3Sb_5 family. A very small $T_c \sim 0.0008$ K in CsV_3Sb_5 has been indeed predicted based on the McMillan equation³³, suggesting that electron-phonon coupling alone is not enough to explain the superconducting transition; nematic fluctuation should be considered as an essential ingredient to result in the relatively high $T_c \sim 3.2$ K in CsV_3Sb_5 . In support of this scenario, it should be noted that the T_c values in

KV_3Sb_5 ($T_c = 0.93$ K⁸) and in RbV_3Sb_5 ($T_c = 0.92$ K⁹) are lower than that in CsV_3Sb_5 ($T_c = 3.2$ K). In addition, unlike the Cs variant, a recent study of Sn doping in polycrystalline KV_3Sb_5 and RbV_3Sb_5 revealed single superconducting domes near the suppression of the CDW orders⁴⁰. All these results, if interpreted correctly, potentially indicate that nematic order and its fluctuations might be absent in both compounds, motivating similar experiments for these materials. Furthermore, our scenario supports that nematic fluctuations should be also considered an important factor to understand the double superconducting domes reported in pressurised CsV_3Sb_5 ^{24,25} and in $\text{CsV}_3\text{Sb}_{5-x}\text{Sn}_x$ ²³ polycrystals.

It should be pointed out that the experimental results found here well resemble those found in the Fe-based superconductors, e.g., $\text{Ba}(\text{Fe}_{1-x}\text{Co}_x)_2\text{As}_2$ ²⁷, $\text{LaFe}_{1-x}\text{Co}_x\text{AsO}$ ²⁹ and $\text{Fe}(\text{Se}_{1-x}\text{Te}_x)$ ³⁰, where unconventional superconductivity is optimised near the NQCP. However, the microscopic origin for having the nematic order seems to be quite different; in contrast to the iron-based superconductors where the spin density wave order is closely coupled to the nematic order^{27–30,41}, the nematic order in CsV_3Sb_5 is intertwined with the unconventional CDW order, possibly in a form of charge bond order^{3,14,18}. Recent theoretical studies^{3,18} considering the kagome-Hubbard model have indeed shown that a triple- \mathbf{q} -charge bond order is stabilised below T_{CDW} , described by three complex CDW order parameters. Furthermore, those theories suggest that these CDW order parameters can undergo a continuous variation of their phases at T_{nem} from a triply-degenerate, isotropic phase of $\pi/2$ into two different values, without the change of the isotropic amplitude, thereby resulting in one-dimensional nematic modulation. Therefore, if the charge bond order developed in CsV_3Sb_5 is assumed to be still maintained over the significant doping level x , the enhanced nematic correlation might be linked to the quantum phase transition involving a continuous variation of the phases of the triple- \mathbf{q} CDW order parameters, at which the charge bond order with anisotropic phases, thus called nematic charge bond order, develops from the one with a homogenous phase.

Several other theoretical investigations considering the kagome-Hubbard model have also predicted that CsV_3Sb_5 might have unconventional superconductivity with a superconducting gap function of s - or p - or d -wave type when the CDW state is melted^{1,17}, possibly via suppression of the amplitudes in the three \mathbf{q} -charge bond orders. Investigations on the superconducting order parameters at the doping level $x = -0.0075$ – 0.01 near the NQCP (first dome) and $x = -0.05$ (second dome) may thus provide an opportunity for studying comparative characteristics of superconductivity instigated by anisotropic phase fluctuations and amplitudes of the three \mathbf{q} -charge bond orders, respectively.

In conclusion, our experimental findings coherently suggest that an NQCP is located near $x = -0.009$ – 0.01 . Moreover, a maximum $T_c = -4.1$ K with full Meissner shielding is realised at $x = -0.0075$ – 0.01 , forming the first superconducting dome near the NQCP. This not only points out the vital role of nematic fluctuation in enhancing superconductivity but also provides important insights into understanding the link between the multiple orders and superconductivity in CsV_3Sb_5 and related kagome superconductors.

Methods

Single crystal growth

$\text{Cs}(\text{V}_{1-x}\text{Ti}_x)_3\text{Sb}_5$ ($0 \leq x \leq 0.06$) single crystals were grown by the Cs-Sb flux method. A mixture of Cs chunks (99.8%, Alfa Aesar), V powders (99.9%, Sigma Aldrich), Ti powders (99.99%, Alfa Aesar) and Sb shots (99.999%, Alfa Aesar) with a molar ratio of Cs: (V, Ti): Sb = 2: 1: 3 were put in an alumina crucible and were double-sealed in an evacuated quartz ampule with pressures less than 2×10^{-5} mbar. The sealed ampules were heated at a rate of 100 °C/h and kept at 1000 °C for 24 h to fully dissolve the V and Ti into the Cs-Sb eutectic mixture. Later, the ampoules were cooled down to 600 °C at a rate of 2 °C/h. At 600 °C, the ampoules were centrifuged to separate the crystals from the molten flux.

To avoid oxidation, all the sample preparation was done inside a glove box, which was kept in an Ar atmosphere with oxygen and moisture concentrations less than 1 ppm. Shiny plate-like crystals were obtained with a typical lateral area of $3 \times 2 \text{ mm}^2$. The CsV_3Sb_5 single crystals exhibited a residual resistivity ratio (RRR) value as high as 129.2.

In-plane resistivity and magnetisation measurements

In-plane resistivity measurements were performed in the PPMS™ using a conventional four-probe method. The electrical contacts were attached by silver paint (Dupont 4929 N). The M/H after zero-field cooling (ZFC) were obtained by MPMS™ (Quantum Design) at temperatures between 5 and 300 K, while the magnetic susceptibility χ between 1.8 and 5 K were measured by a vibrating sample magnetometer in a PPMS™ (Quantum Design). The demagnetisation factors in the M/H and χ measurements have been corrected after measuring the samples in a needle-like configuration.

Elastoresistance measurements

The elastoresistance was measured in a closed-cycle cryostat (Sumitomo RDK-101D) using a commercial piezoelectric actuator (Piezomechanik Pst 150) at various temperatures from 6 to 250 K. The samples were glued to the piezoelectric actuator by using an adhesive epoxy (Devcon 14250). Two samples were cut in rectangular shapes with a lateral size of $-1 \times 0.2 \text{ mm}^2$; the longer direction was parallel (perpendicular) to the a -axis for the R_{xx} (R_{yy}) sample. All the samples were cleaved to the thickness of $\sim 20 \mu\text{m}$ to ensure efficient strain transmission to the entire sample. The electrical contacts were attached directly by silver paint (Dupont 4929 N) to the freshly cleaved surface. Two strain gauges were glued on the other side of the actuator with perpendicular orientation to each other.

X-ray diffraction and wavelength dispersive X-ray spectroscopy measurements

$\text{Cs}(\text{V}_{1-x}\text{Ti}_x)_3\text{Sb}_5$ single crystals were ground and inserted inside a quartz capillary tube with an inner diameter of 0.5 mm. The tube was measured by x-ray diffraction (XRD) θ - 2θ scans using a high-resolution x-ray diffractometer (PANalytical Empyrean). Wavelength dispersive x-ray spectroscopy (WDS) were performed in a field emission electron probe microanalyzer (JEOL Ltd., JXA-8530F) by taking V (99.99%), Ti (99.9%) and Sb (99.99%) metals as standard specimens. The standard specimen data of Cs was taken from the JEOL database due to the high air sensitivity of the elemental Cs metal.

Data availability

Source data are provided with this paper. The data generated in this study have been deposited in the Figshare database⁴².

References

- Wang, W.-S., Li, Z.-Z., Xiang, Y.-Y. & Wang, Q.-H. Competing electronic orders on kagome lattices at van Hove filling. *Phys. Rev. B* **87**, 115135 (2013).
- Kiesel, M. L., Platt, C. & Thomale, R. Unconventional Fermi surface instabilities in the kagome Hubbard model. *Phys. Rev. Lett.* **110**, 126405 (2013).
- Denner, M. M., Thomale, R. & Neupert, T. Analysis of charge order in the kagome metal AV_3Sb_5 ($A = \text{K}, \text{Rb}, \text{Cs}$). *Phys. Rev. Lett.* **127**, 217601 (2021).
- Yu, S. -L. & Li, J. -X. Chiral superconducting phase and chiral spin-density-wave phase in a Hubbard model on the kagome lattice. *Phys. Rev. B* **85**, 144402 (2012).
- Jiang, Y.-X. et al. Unconventional chiral charge order in kagome superconductor KV_3Sb_5 . *Nat. Mater.* **20**, 1353 (2021).
- Shumiya, N. et al. Intrinsic nature of chiral charge order in the kagome superconductor RbV_3Sb_5 . *Phys. Rev. B* **104**, 035131 (2021).
- Wang, Z. et al. Electronic nature of chiral charge order in the kagome superconductor CsV_3Sb_5 . *Phys. Rev. B* **104**, 075148 (2021).
- Ortiz, B. R. et al. Superconductivity in the Z_2 kagome metal KV_3Sb_5 . *Phys. Rev. Mater.* **5**, 034801 (2021).
- Yin, Q. et al. Superconductivity and normal-state properties of kagome metal RbV_3Sb_5 single crystals. *Chin. Phys. Lett.* **38**, 037403 (2021).
- Ortiz, B. R. et al. CsV_3Sb_5 : a Z_2 topological kagome metal with a superconducting ground state. *Phys. Rev. Lett.* **125**, 247002 (2020).
- Liang, Z. et al. Three-dimensional charge density wave and surface-dependent vortex-core states in a kagome superconductor CsV_3Sb_5 . *Phys. Rev. X* **11**, 031026 (2021).
- Ortiz, B. R. et al. Fermi surface mapping and the nature of charge-density-wave order in the kagome superconductor CsV_3Sb_5 . *Phys. Rev. X* **11**, 041030 (2021).
- Miao, H. et al. Geometry of the charge density wave in the kagome metal AV_3Sb_5 . *Phys. Rev. B* **104**, 195132 (2021).
- Nie, L. et al. Charge-density-wave-driven electronic nematicity in a kagome superconductor. *Nature* **604**, 59–64 (2022).
- Park, T., Ye, M. & Balents, L. Electronic instabilities of kagome metals: Saddle points and Landau theory. *Phys. Rev. B* **104**, 035142 (2021).
- Wu, X. et al. Nature of unconventional pairing in the kagome superconductors AV_3Sb_5 ($A = \text{K}, \text{Rb}, \text{Cs}$). *Phys. Rev. Lett.* **127**, 177001 (2021).
- Tazai, R., Yamakawa, Y., Onari, S. & Kontani, H. Mechanism of exotic density-wave and beyond-Migdal unconventional superconductivity in kagome metal AV_3Sb_5 ($A = \text{K}, \text{Rb}, \text{Cs}$). *Sci. Adv.* **8**, eabl4108 (2022).
- Tazai, R., Yamakawa, Y. & Kontani, H. Charge-loop current order and Z_3 nematicity mediated by bond-order fluctuations in kagome metal AV_3Sb_5 ($A = \text{Cs}, \text{Rb}, \text{K}$). Preprint at <https://doi.org/10.48550/arXiv.2207.08068> (2022).
- Zhao, C. C. et al. Nodal superconductivity and superconducting domes in the topological Kagome metal CsV_3Sb_5 . Preprint at <https://doi.org/10.48550/arXiv.2102.08356> (2021).
- Chen, H. et al. Roton pair density wave in a strong-coupling kagome superconductor. *Nature* **599**, 222–228 (2021).
- Duan, W. et al. Nodeless superconductivity in the kagome metal CsV_3Sb_5 . *Sci. China. Phys. Mech. Astron.* **64**, 107462 (2021).
- Gupta, R. et al. Microscopic evidence for anisotropic multigap superconductivity in the CsV_3Sb_5 kagome superconductor. *npj Quantum Mater.* **7**, 49 (2022).
- Oey, Y. M. et al. Fermi level tuning and double-dome superconductivity in the kagome metal $\text{CsV}_3\text{Sb}_{5-x}\text{Sn}_x$. *Phys. Rev. Mater.* **6**, L041801 (2022).
- Chen, K. Y. et al. Double superconducting dome and triple enhancement of T_c in the kagome superconductor CsV_3Sb_5 under high pressure. *Phys. Rev. Lett.* **126**, 247001 (2021).
- Yu, F. H. et al. Unusual competition of superconductivity and charge-density-wave state in a compressed topological kagome metal. *Nat. Commun.* **12**, 3645 (2021).
- Chu, J.-H., Kuo, H.-H., Analytis, J. G. & Fisher, I. R. Divergent nematic susceptibility in an iron arsenide superconductor. *Science* **337**, 710–712 (2012).
- Kuo, H.-H., Chu, J.-H., Palmstrom, J. C., Kivelson, S. A. & Fisher, I. R. Ubiquitous signatures of nematic quantum criticality in optimally doped Fe-based superconductors. *Science* **352**, 958–962 (2016).
- Hosoi, S. et al. Nematic quantum critical point without magnetism in $\text{FeSe}_{1-x}\text{S}_x$ superconductors. *Proc. Natl Acad. Sci. USA* **113**, 8139 (2016).
- Hong, X. et al. Evolution of the nematic susceptibility in $\text{LaFe}_{1-x}\text{Co}_x\text{AsO}$. *Phys. Rev. Lett.* **125**, 067001 (2020).

30. Ishida, K. et al. Pure nematic quantum critical point accompanied by a superconducting dome. *Proc. Natl Acad. Sci. USA* **119**, e2110501119 (2022).
31. Yang, H. et al. Titanium doped kagome superconductor $\text{CsV}_{3-x}\text{Ti}_x\text{Sb}_5$ and two distinct phases. *Sci. Bull.* **67**, 2176 (2022).
32. Liu, Y. et al. Doping evolution of superconductivity, charge order and band topology in hole-doped topological kagome superconductors $\text{Cs}(\text{V}_{1-x}\text{Ti}_x)_3\text{Sb}_5$. *Phys. Rev. Materials* **7**, 064801 (2023).
33. Tan, H., Liu, Y., Wang, Z. & Yan, B. Charge density waves and electronic properties of superconducting kagome metals. *Phys. Rev. Lett.* **127**, 046401 (2021).
34. Kim, C. et al. Experimental signatures of nodeless multiband superconductivity in a 2H-Pd_{0.08}TaSe₂ single crystal. *Sci. Rep.* **11**, 13383 (2021).
35. Wang, B. et al. Pressure-induced bulk superconductivity in a layered transition-metal dichalcogenide 1T-tantalum selenium. *Phys. Rev. B* **95**, 220501 (R) (2017).
36. Gruner, T. et al. Charge density wave quantum critical point with strong enhancement of superconductivity. *Nat. Phys.* **13**, 967–972 (2017).
37. Kuo, H. –H., Shapiro, M. C., Riggs, S. C. & Fisher, I. R. Measurement of the elastoresistivity coefficients of the underdoped iron arsenide $\text{Ba}(\text{Fe}_{0.975}\text{Co}_{0.025})_2\text{As}_2$. *Phys. Rev. B* **88**, 085113 (2013).
38. Luo, J. et al. Possible star-of-David pattern charge density wave with additional modulation in the kagome superconductor CsV_3Sb_5 . *npj Quantum Mater.* **7**, 30 (2022).
39. Eckberg, C. et al. Sixfold enhancement of superconductivity in a tunable electronic nematic system. *Nat. Phys.* **16**, 346–350 (2020).
40. Oey, Y. M., Kaboudvand, F., Ortiz, B. R., Seshadri, R. & Wilson, S. D. Tuning charge density wave order and superconductivity in the kagome metals $\text{KV}_3\text{Sb}_{5-x}\text{Sn}_x$ and $\text{RbV}_3\text{Sb}_{5-x}\text{Sn}_x$. *Phys. Rev. Mater.* **6**, 074802 (2022).
41. Fernandes, R. M., Chubukov, A. V. & Schmalian, J. What drives nematic order in iron-based superconductors? *Nat. Phys.* **10**, 97–104 (2014).
42. Sur, Y., Kim, K. –T., Kim, S. & Kim, K. H. Optimized superconductivity in the vicinity of a nematic quantum critical point in the kagome superconductor $\text{Cs}(\text{V}_{1-x}\text{Ti}_x)_3\text{Sb}_5$ data sets. figshare <https://doi.org/10.6084/m9.figshare.22808321> (2023).

Acknowledgements

Y.S., K.–T.K., S.K. and K.H.K. were financially supported by the Ministry of Science and ICT through the National Research Foundation of Korea (2019R1A2C2090648, 2022H1D3A3A01077468) and by the Ministry of Education (2021R1A6C101B418).

Author contributions

Y.S. and K.H.K. initiated the project. Y.S., K.–T.K. and S.K. prepared the single crystalline samples. Y.S. characterised the samples and performed the measurements. Y.S. and K.H.K. analysed the data and wrote the manuscript. K.H.K. devised the project and advised the research. All authors discussed the results and commented on the manuscript.

Competing interests

The authors declare no competing interests.

Additional information

Supplementary information The online version contains supplementary material available at <https://doi.org/10.1038/s41467-023-39495-1>.

Correspondence and requests for materials should be addressed to Kee Hoon Kim.

Peer review information *Nature Communications* thanks the anonymous reviewer(s) for their contribution to the peer review of this work. A peer review file is available.

Reprints and permissions information is available at <http://www.nature.com/reprints>

Publisher's note Springer Nature remains neutral with regard to jurisdictional claims in published maps and institutional affiliations.

Open Access **Open Access** This article is licensed under a Creative Commons Attribution 4.0 International License, which permits use, sharing, adaptation, distribution and reproduction in any medium or format, as long as you give appropriate credit to the original author(s) and the source, provide a link to the Creative Commons licence, and indicate if changes were made. The images or other third party material in this article are included in the article's Creative Commons licence, unless indicated otherwise in a credit line to the material. If material is not included in the article's Creative Commons licence and your intended use is not permitted by statutory regulation or exceeds the permitted use, you will need to obtain permission directly from the copyright holder. To view a copy of this licence, visit <http://creativecommons.org/licenses/by/4.0/>.

© The Author(s) 2023